An Anti-Biofouling Flexible Fiber Biofuel Cell Working in the Brain

Yue Guo, Chuanrui Chen, Jianyou Feng, Liyuan Wang, Jiajia Wang, Chengqiang Tang, Xuemei Sun,* and Huisheng Peng*

Biofuel cell (BFC) that transfers chemical energy into electricity is a promising candidate as an energy-harvesting device for implantable electronics. However, there still remain major challenges for implantable BFCs, including bulky and rigid device structure mismatching with soft tissues such as the brain, and the power output decreases due to the fouling process in a biological environment. Here, a flexible and anti-biofouling fiber BFC working in the brain chronically is developed. The fiber BFC is based on a carbon nanotube fiber electrode to possess small size and flexibility. A hydrophilic zwitterionic anti-biofouling polydopamine-2-methacryloyloxyethyl phosphorylcholine layer is designed on the surface of fiber BFC to resist the nonspecific protein adsorption in a complex biological environment. After implantation, the fiber BFC can achieve a stable device/tissue interface, along with a negligible immune response. The fiber BFC has first realized power generation in the mouse brain for over a month, exhibiting its promising prospect as an energy-harvesting device in vivo.

1. Introduction

Neuroscience is in rapid development with the goal of understanding the brain function and developing therapies for neurological diseases.[1] Significant efforts have been made to develop advanced implantable electronics, such as neural probes, optoelectronics, and electrochemical sensors for aiding neuroscience research.[2–4] These electronic devices are traditionally powered by batteries or wireless power transfer systems.[2] Harvesting energy from biofuels in vivo is an alternative promising strategy for powering these implantable electronics, since the biofuels are abundant and continuously replenished in the living body. Biofuel cell (BFC) is such an energy-harvesting device by transforming chemical energy into electricity.[5–13] It is normally constructed by two electrodes modified with enzymatic or metallic

catalysts, where the redox reactions drive the electron transfer and thus generate electrical power.[14–16] Till now, there have been some advances reporting wearable integrated electronic systems using BFC as an energy source, which offer promise to construct next-generation wearable electronics for healthcare and personalized medicine.[17–19]

Unfortunately, for implantable applications, especially when operating in soft and delicate regions such as the brain, there still remain major challenges for BFCs. First, most of the reported BFCs were based on 3D bulky structures, which made them difficult to be implanted and may create large surgical wounds during implantation. Also, this restricted their operation positions to the abdominal cavity for mammals in most cases.[8–10] To tackle this problem, fiber BFCs have been developed as implantable energy-harvesting devices. Due to their 1D structure and small size, they can be implanted into deep tissues, such as the brain[11] and blood vessels.[12,13] However, these fiber BFCs were usually based on carbon fibers or gold wires. These materials were stiff or brittle, and they did not mechanically match soft tissues in living creatures, which may cause severe foreign body reactions.[20,21] In addition, the efficiency and stability of BFC energy supply were impaired by biofouling, a biological process caused by adsorption and accumulation of biomolecules on implanted devices.[22–28] These aforementioned problems limited the in vivo applications of BFCs.

In this manuscript, we report a flexible and anti-biofouling fiber BFC that can work in the brain with stable power output in the long term. The fiber BFC is constructed based on an intrinsic flexible carbon nanotube (CNT) fiber electrode, which is biocompatible[29,30] and mechanically match with soft biological tissues,[30,31] and thus commonly used for fabricating neural probes[32,33] and implantable electrochemical sensor.[30,34,35] The simple in situ polymerized hydrophilic zwitterionic polydopamine-2-methacryloyloxyethyl phosphorylcholine (PDA-MPC) layer modified on fiber BFC enables its resistance to nonspecific protein adsorption and maintenance of power output in complex biological fluids. As a result, the fiber BFC demonstrated its good biocompatibility and long-term stability after being implanted into the mouse brain for 1 month.

Y. Guo, C. Chen, J. Feng, L. Wang, J. Wang, C. Tang, X. Sun, H. Peng
State Key Laboratory of Molecular Engineering of Polymers
Department of Macromolecular Science, and Laboratory of
Advanced Materials
Fudan University
Shanghai 200438, China
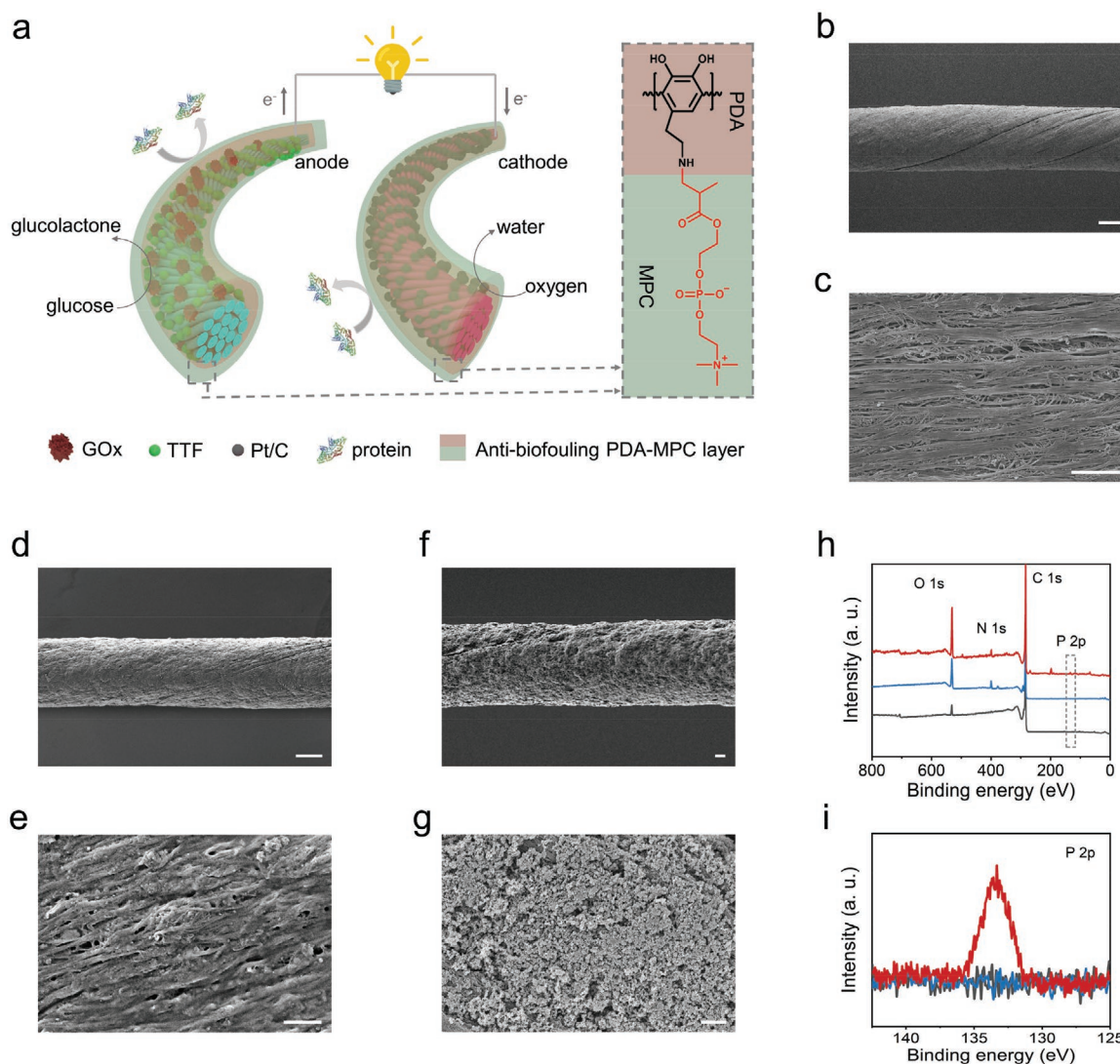E-mail: sunxm@fudan.edu.cn; penghs@fudan.edu.cn

Figure 1. Schematic diagram and characterization of fiber BFC. a) Schematic diagram of construction and reaction mechanism of fiber BFC. b,c) SEM images of bare CNT fiber electrode at low and high magnifications, respectively. Scale bar, b) 30 μm; c) 1 μm. d,e) SEM images of fiber bioanode at low and high magnifications, respectively. Scale bar, d) 30 μm; e) 1 μm. f,g) SEM images of fiber cathode at low and high magnifications, respectively. Scale bar, f) 30 μm; g) 1 μm. h) XPS spectra of PDA-MPC modified (red curve), PDA modified (blue curve), and bare CNT fiber electrodes (gray curve). i) High-resolution XPS spectra of P 2p peak of PDA-MPC modified (red curve), PDA modified (blue curve), and bare CNT fiber electrodes (gray curve).

2. Results and Discussion

Since glucose and oxygen are the most widely distributed biofuels for energy metabolism in body fluid, here we constructed the glucose/oxygen BFCs toward implantable applications. The electrode design and reaction mechanism are illustrated in **Figure 1**a. The CNT fiber was chosen as a flexible electrode substrate, which can be synthesized by floating catalyst chemical vapor deposition at a large scale (Figure S1a, Supporting Information). The CNT fiber was flexible and can maintain its structural integrity even after being knotted (Figures S1b and S2, Supporting Information). The glucose oxidase (GOx) and platinum on carbon (Pt/C) were chosen as catalysts to be immobilized on the CNT fiber electrodes to enable the redox reaction of biofuels (glucose and oxygen). Both of the catalysts are high-performance and commercially available, and

thus extensively used for biosensing and biofuel cell.[17,19,36–38] On fiber bioanode, tetrathiafulvalene (TTF) was adopted as a mediator for shuttling electrons between the redox center of enzyme and CNT fiber electrode,[39] and then GOx was immobilized through glutaraldehyde crosslinking to catalyze glucose to glucolactone. The Pt/C catalyst was modified on a fiber cathode in order to reduce oxygen to water. To endow the fiber BFC with anti-biofouling performance, a hydrophilic zwitterionic PDA-MPC layer was designed and fabricated via simple in situ chemical reactions (Figure S3, Supporting Information). Briefly, the electrodes were first immersed in dopamine solution, which lead to PDA formation on the electrodes by oxidative self-polymerization of dopamine.[40] Later, the electrodes were treated by MPC solution, leading to the conjugation between the amine groups of PDA and acrylate zwitterionic MPC molecules via Michael addition.[41]

**ADVANCED
SCIENCE NEWS**

www.advancedsciencenews.com

**small
methods**

www.small-methods.com

Scanning electron microscope (SEM) images of fiber bio-anode (Figure 1d,e) and cathode (Figure 1f,g) were taken to show the morphology and distribution of active materials on CNT fiber electrodes. SEM images of bare CNT fiber electrode (Figure 1b,c) showed its porous structure originated from the nanoscale gaps among CNT bundles, which can provide large surface areas and thus enable high loading amount of active materials. Figure 1e shows the cross-linked enzyme was homogeneously covered on CNT bundles, which enabled efficient electron transfer among enzyme, mediator, and electrode. The nanoparticles observed in Figure 1g and Figure S4 (Supporting Information) can be attributed to Pt/C catalyst, which were packed densely and uniformly on CNT fiber electrode. The SEM images of PDA-MPC modified and unmodified electrodes showed no significant difference (Figure S5, Supporting Information), possibly because of the ultrathin thickness of the PDA-MPC layer on fiber electrodes. Analysis by atomic force microscopy suggested the thickness of the PDA-MPC layer was only ≈5 nm (Figure S6, Supporting Information). In order to confirm the successful modification of the PDA-MPC layer, X-ray photoelectron spectroscopy (XPS) analysis was performed on PDA-MPC modified, PDA-modified, and bare CNT fiber electrodes. As shown in Figure 1h,i, after PDA formation, a new peak at 399.7 eV was shown, which was ascribed to the binding energy of N 1s. After the following MPC modification, there further appeared a new peak at 133.2 eV (P 2p peak), which indicated a successful chemical reaction between MPC and PDA.

The electrochemical performance of fiber bioanode and cathode was evaluated using a three-electrode system with a platinum wire counter electrode and a Ag/AgCl reference electrode. Linear sweep voltammograms (LSVs) were performed to indicate the occurrence of glucose oxidation and oxygen reduction on fiber anode and cathode, respectively (**Figure 2**a,b). Through modulating the enzyme concentrations and loading amounts of catalysts modified on electrodes, the electrochemical performance of fiber bioanode and cathode can be optimized (Figure S7, Supporting Information). The optimal conditions were selected as 40 mg mL^{-1} GOx solution for bioanode and 0.44 mg cm^{-2} of Pt/C catalyst for the cathode. In addition, since the cathodic current density was lower than the anodic current density (Figure S7, Supporting Information), the area of the cathode was designed to be twice as that of bioanode to ensure the power output of BFC was not limited by the oxygen reduction reaction on the cathode. It is expected that the additional modification layer on fiber electrodes should not compromise the power output of BFC. Thus, the impacts of PDA-MPC modification on the electrochemical properties of bare CNT fiber electrode, fiber bioanode, and cathode were evaluated. The cyclic voltammetry performance of PDA-MPC modified and unmodified CNT fiber electrodes in potassium ferricyanide was investigated (Figure S8, Supporting Information). It appeared that the PDA-MPC modified electrode had a higher capacitive current and similar redox peak current compared to the unmodified one, indicating that the PDA-MPC modification did not impede mass transport or electron transfer process, which might be attributed to the ultrathin feature of the PDA-MPC layer. As shown in Figure S9 (Supporting Information), PDA-MPC modified fiber bioanode showed higher overpotential (≈60 mV) than unmodified one, but they reached nearly the same oxidative current density at 0.15 V. As for cathode, the PDA-MPC modified one showed a lower overpotential of the oxygen reduction reaction.

The power output performance of fiber BFC was investigated using a two-electrode system with fiber cathode as the working
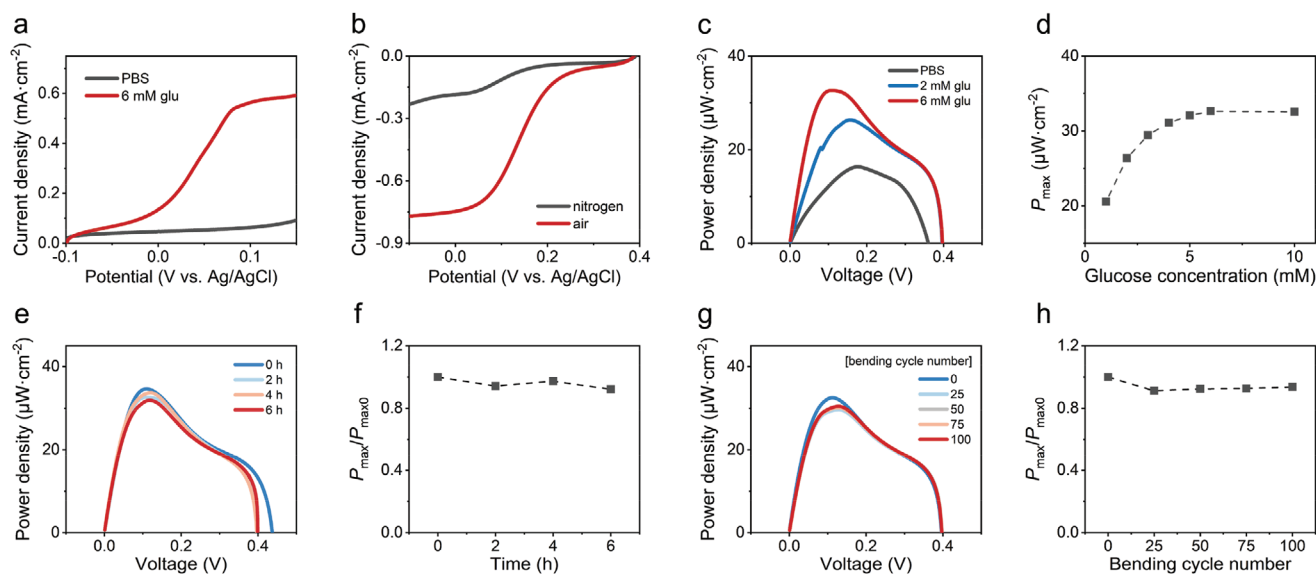

Figure 2. Electrochemical performance of fiber BFC. a) LSVs of fiber bioanode in phosphate buffer saline (PBS) and glucose solution (glu) at 5 mV s^{-1}. b) LSVs of fiber cathode in air-saturated and nitrogen-saturated PBS at 5 mV s^{-1}. c) The power density–voltage curves of fiber BFC in different concentrations of glucose. d) Corresponding maximal power density–glucose concentration calibration plot. e) The power density–voltage curves of fiber BFC in glucose solution at different periods. f) The calculated relative change of maximal power density of fiber BFC over 6 h. g) The power density–voltage curves of fiber BFC bending at 30° for 0, 25, 50, 75, and 100 cycles. h) The calculated relative change of maximal power density of fiber BFC over 100 bending cycles.

electrode and fiber bioanode as the counter and reference electrode, and LSVs were recorded in different concentrations of glucose solution. The maximal power density increased when the glucose concentration increased over the range of 0–6×10^{-3} м, and then reached the saturated point at $\approx 6 \times 10^{-3}$ м of glucose, where a maximal power density of 32.6 µW cm^{-2} was obtained (Figure 2c,d). As a proof-of-concept, the fiber BFC was integrated with a strain sensor[42] in vitro into a self-powered sensing system. A distinguishable signal can be recorded according to the change of strain (Figure S10, Supporting Information), demonstrating the feasibility of combining the fiber BFC with sensors to construct a functional system for future use.

It is a necessity for BFCs to stably generate power over periods of time for practical usage. In this regard, the stability of power output of fiber BFC was investigated by performing LSVs in glucose solution over a period of 6 h (Figure 2e). As shown in Figure 2f, the maximal power density of fiber BFC maintained over 92% during the period. As for implantable applications, it is known that the brain tissue in the living body bears constant micromovements due to respiration and heartbeat,[43] which raises the requirement for implantable electronics to perform stably under repeated deformations. The mechanical stability of fiber BFC performance was monitored by performing LSVs after every 25 cycles of bending at 30°. As shown in Figure 2g,h, the maximal power density of fiber BFC maintained over 91% during 100 cycles of bending. The maximal power density of fiber BFC bending at different angles also remained stable (Figure S11, Supporting Information), which validated the mechanical stability of the fiber BFC as a practical implantable energy-harvesting device.

The anti-biofouling performance of fiber BFC must be seriously considered for the capability for prolonged implantation. It has been widely accepted that the implanted electrodes inevitably suffer from nonspecific adsorption of proteins and cells (that is, biofouling) immediately when the implants are in contact with biological components, which causes the continuous device performance deterioration within several hours. The biofouling processes will further trigger foreign body reaction and lead to the formation of a fibrous capsule on implanted devices, which severely hinders substrates from reaching the electrode and hence inactivates the implanted electrochemical devices.[22–28] As a consequence, the biofouling processes will restrict the availability of fuel at the BFC electrodes, leading to reduction of power output. To investigate the anti-biofouling performance of fiber BFC, its power output was recorded before and after incubation in 10 mg mL^{-1} bovine serum albumin (BSA) solution. After incubation in BSA solution, the discharge curves of PDA-MPC modified and unmodified fiber BFCs were immediately recorded (**Figure 3**a). It showed that PDA-MPC modified fiber BFC generated higher power output. The LSVs of PDA-MPC modified and unmodified fiber BFCs were recorded after incubation in BSA solution for a longer time. The maximal power density of PDA-MPC modified fiber BFC was maintained by ≈70% of the initial value after incubation in BSA solution for 2 h, while that of unmodified fiber BFC dropped down to 55% (Figure 3b).

The excellent anti-biofouling performance of fiber BFC can be attributed to the hydrophilicity of PDA-MPC modification. As shown in Figure 3c, the water contact angle of the PDA-MPC modified electrode was 13°, lower than that of PDA modified (42°) and bare electrode (116°), indicating that PDA-MPC modified electrode was the most hydrophilic and thus had the ability of resisting nonspecific protein binding in a complex biological environment. Furthermore, the nonspecific protein binding of PDA-MPC modified, PDA modified and bare electrodes were characterized by immersing them into fluorescein isothiocyanate-tagged BSA (FITC-BSA) solution for 2 h. As
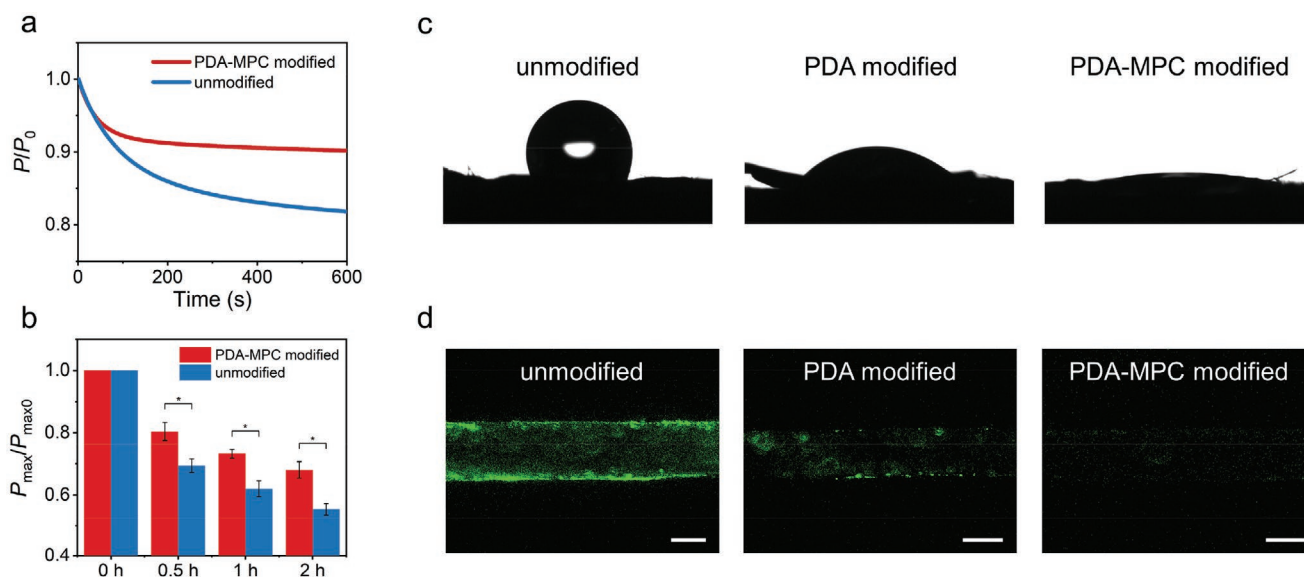

Figure 3. The anti-biofouling performance of fiber BFC and its mechanism. a) The power output change at 2 µA cm^{-2} of PDA-MPC modified and unmodified BFCs after incubation in 10 mg mL^{-1} BSA immediately. b) The calculated relative changes of the maximal power density of PDA-MPC modified and unmodified BFCs after incubation in 10 mg mL^{-1} BSA for 0.5, 1, and 2 h. All values represent means ± standard deviations ($n = 3$; *$p < 0.05$, paired two-sided Student's t-test) c) The water contact angles of unmodified, PDA modified and PDA-MPC modified CNT electrodes. d) Confocal fluorescence microscopy images of FITC-BSA treated unmodified, PDA modified and PDA-MPC modified CNT electrodes. Scale bar, 30 µm.
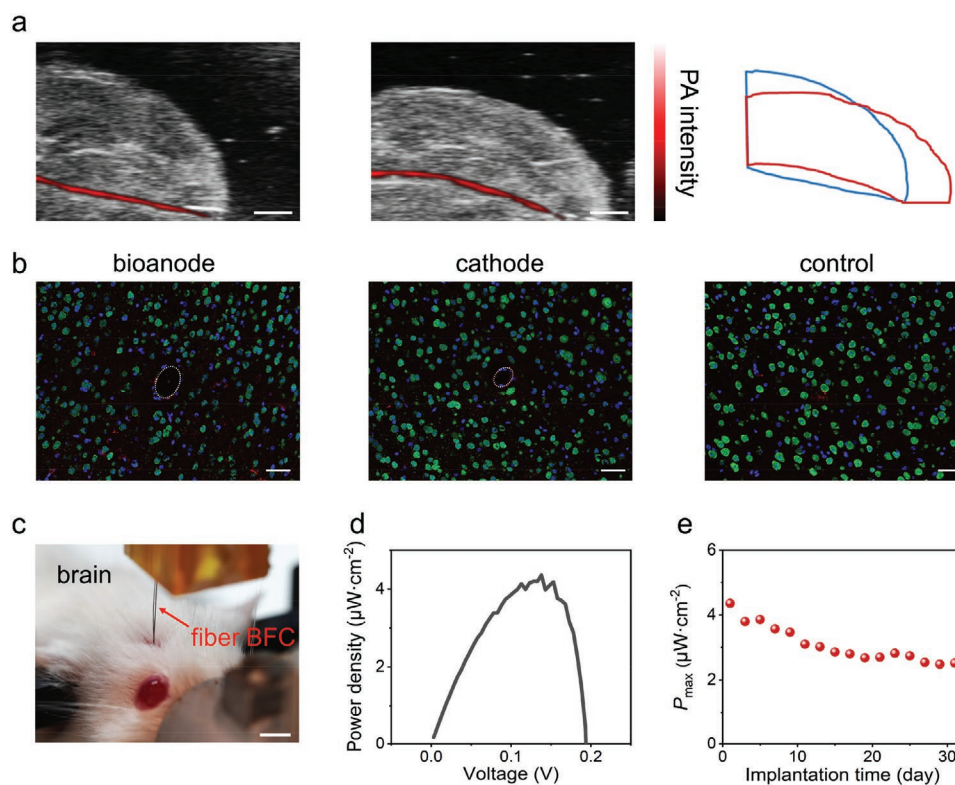
Figure 4. The mechanical match demonstration, biocompatibility, and in vivo performance of fiber BFC. a) Photoacoustic (PA) images of the mouse brain implanted with a fiber electrode before (left) and after (middle) compression. The contour lines (right) were extracted from PA images. Scale bar, 1 mm. b) Immunohistochemical staining images of cross-sectional brain slices at 1 month after implantation of fiber BFC. Blue, red, and green colors correspond to DAPI (label of cell nuclei), GFAP (label of astrocytes), and NeuN (label of neuron somata), respectively. The white dotted circles indicate the position of fiber bioanode or cathode. Scale bar, 50 μm. c) Photograph showing the implantation of fiber BFC electrode into the mouse brain through tungsten wire-assisted strategy. Scale bar, 1 cm. d) The power density–voltage curve of PDA-MPC modified fiber BFC in the mouse brain on the first day after implantation. e) The maximal power density of PDA-MPC modified BFC generated in vivo for over a month.

shown in Figure 3d, no sign of massive protein adsorption was observed on the PDA-MPC modified electrode. In contrast, the bare electrode showed bright green fluorescence, which manifested the prominent adsorption of proteins onto the electrode.

For implantable applications, the soft devices can reduce foreign body reaction and irreversible tissue damages compared to their rigid counterparts, as well as retain stable performance during operation in dynamic biological tissues.[20,21] The intrinsic flexibility of the CNT fiber electrode made the fiber BFC feasible as an implantable device. The bending stiffness of the CNT fiber was close to those of the biological tissues, which indicated that it could mechanically match soft tissues and thus establish a stable device/tissue interface.[30,31,34] To obtain the dynamic interface between fiber BFC electrode and the mouse brain under deformation, a fiber BFC electrode was implanted into the mouse brain, and photoacoustic (PA) images were collected before and after a compression was applied to the brain (**Figure 4**a). It indicated that the fiber electrode bent along with the compression deformation of the mouse brain, and achieved a stable device/tissue interface. In addition, the internal stress of the CNT fiber electrode under deformation was measured by recording force–compression curves (Figure S12a, Supporting Information). The results showed that the internal stress of CNT fiber

was more than one order of magnitude lower than that of carbon fiber and gold wire (Figure S12b, Supporting Information). It demonstrated that CNT fiber electrodes would cause the minimal shearing force to the surrounding tissues under deformation, thus having the potential of reducing immune response after implantation.

To further evaluate the immune response of fiber BFC, immunohistochemical staining was adopted to analyze the cell distribution around fiber BFC after being implanted into the mouse brain for 1 week and 1 month (Figure 4b, Figures S13 and S14, Supporting Information). The cross-sectional brain slices were stained with monoclonal antibodies for glial fibrillary acidic protein (GFAP), ionized calcium-binding adapter molecule (Iba-1), and neuronal nuclear antigen (NeuN) to label astrocytes, microglia, and neuron somata, respectively. In addition, the cell nuclei were stained by 4′,6-diamidino-2-phenylindole (DAPI). Fluorescence microscopy images showed that the expression of GFAP, Iba-1, and NeuN around the devices had no significant difference compared with that of a control group without implantation. It indicated that there was no obvious accumulation of astrocytes and microglia or the depletion of neurons around the implanted fiber BFC. These results demonstrated the fiber BFC elicited negligible immune response after implantation and thus had good biocompatibility.

Furthermore, the fiber BFC was implanted into the mouse brain (Figure 4c) to validate its efficacy and stability as an energy-harvesting device in vivo. The fiber BFC could generate a power density of ≈4.4 µW cm^{-2} in the mouse brain (Figure 4d). The power density and open-circuit voltage of fiber BFC in vivo were lower than those in vitro, possibly because the concentration of oxygen in the brain was lower than that in the air-saturated solution.[44] The discharge curves of PDA-MPC modified and unmodified fiber BFCs in vivo were recorded. The power output of PDA-MPC modified fiber BFC was stable, while that of unmodified one decreased remarkably during the same period (Figures S15 and S16, Supporting Information). It was possibly because of the more severe adsorption of protein on the surface of unmodified electrodes (Figures S17 and S18, Supporting Information). In order to evaluate the stability of the PDA-MPC modification layer during implantation, XPS analysis was performed on PDA-MPC modified electrodes before and after implantation (Figure S19, Supporting Information). It showed that the characteristic P 2p peak still existed, indicating the PDA-MPC modification layer on the electrodes remained stable during implantation. To further evaluate the long-term stability of the PDA-MPC modified BFC in vivo, its power output was recorded for over a month (Figure 4e). It showed that the PDA-MPC modified BFC could still generate a power density of ≈2.5 µW cm^{-2} after being implanted for over a month. For comparison, the open-circuit voltage of unmodified BFC decreased to below zero after the first day of implantation, and it could not provide power in vivo thereafter (Figure S20, Supporting Information). These results indicated that PDA-MPC modified BFC had higher resistance to nonspecific adsorption of protein and higher retention of power density than unmodified one. Our fiber BFC has first realized power generation in the mouse brain for over a month (Table S1, S2, Supporting Information), exhibiting its promising prospect as an energy-harvesting device in vivo.

3. Conclusion

In summary, we have developed a flexible and anti-biofouling fiber BFC toward implantable applications in the brain. The flexibility of the fiber BFC enabled it stably generate power under repeated deformations, mechanically match the soft brain tissue and establish a stable device–tissue interface. The hydrophilic zwitterionic PDA-MPC modification endowed the fiber BFC with anti-biofouling performance, resulting in higher power retention in a complex biological environment compared to an unmodified one. After minimal-invasively implanted into the mouse brain, the fiber BFC elicited negligible immune response, while capable of generating power output in long term. Our fiber BFC has first realized power generation in the mouse brain for over a month, exhibiting its promising application prospect for powering implantable electronics and constructing a functional system in vivo.

Supporting Information

Supporting Information is available from the Wiley Online Library or from the author.

[1] S. Brenner, T. J. Sejnowski, *Science* **2011**, *334*, 567.
[2] A. Vazquez-Guardado, Y. Yang, A. J. Bandodkar, J. A. Rogers, *Nat. Neurosci.* **2020**, *23*, 1522.
[3] R. Chen, A. Canales, P. Anikeeva, *Nat. Rev. Mater.* **2017**, *2*, 16093.
[4] G. Hong, C. M. Lieber, *Nat. Rev. Neurosci.* **2019**, *20*, 330.
[5] L. Halamkova, J. Halamek, V. Bocharova, A. Szczupak, L. Alfonta, E. Katz, *J. Am. Chem. Soc.* **2012**, *134*, 5040.
[6] M. Rasmussen, R. E. Ritzmann, I. Lee, A. J. Pollack, D. Scherson, *J. Am. Chem. Soc.* **2012**, *134*, 1458.
[7] D. Lee, S. H. Jeong, S. Yun, S. Kim, J. Sung, J. Seo, S. Son, J. T. Kim, L. Susanti, Y. Jeong, S. Park, K. Seo, S. J. Kim, T. D. Chung, *Biosens. Bioelectron.* **2021**, *171*, 112746.
[8] P. Cinquin, C. Gondran, F. Giroud, S. Mazabrard, A. Pellissier, F. Boucher, J. -P. Alcaraz, K. Gorgy, F. Lenouvel, S. Mathe, P. Porcu, S. Cosnier, *PLoS One* **2010**, *5*, e10476.
[9] A. Zebda, S. Cosnier, J. P. Alcaraz, M. Holzinger, A. Le Goff, C. Gondran, F. Boucher, F. Giroud, K. Gorgy, H. Lamraoui, P. Cinquin, *Sci. Rep.* **2013**, *3*, 1516.
[10] S. El Ichi-Ribault, J. -P. Alcaraz, F. Boucher, B. Boutaud, R. Dalmolin, J. Boutonnat, P. Cinquin, A. Zebda, D. K. Martin, *Electrochim. Acta* **2018**, *269*, 360.
[11] V. Andoralov, M. Falk, D. B. Suyatin, M. Granmo, J. Sotres, R. Ludwig, V. O. Popov, J. Schouenborg, Z. Blum, S. Shleev, *Sci. Rep.* **2013**, *3*, 3270.
[12] T. Miyake, K. Haneda, N. Nagai, Y. Yatagawa, H. Onami, S. Yoshino, T. Abe, M. Nishizawa, *Energy Environ. Sci.* **2011**, *4*, 5008.
[13] F. C. P. F. Sales, R. M. Iost, M. V. A. Martins, M. C. Almeida, F. N. Crespilho, *Lab Chip* **2013**, *13*, 468.
[14] I. Jeerapan, J. R. Sempionatto, J. Wang, *Adv. Funct. Mater.* **2020**, *30*, 1906243.
[15] X. Xiao, H. Xia, R. Wu, L. Bai, L. Yan, E. Magner, S. Cosnier, E. Lojou, Z. Zhu, A. Liu, *Chem. Rev.* **2019**, *119*, 9509.
[16] M. Rasmussen, S. Abdellaoui, S. D. Minteer, *Biosens. Bioelectron.* **2016**, *76*, 91.
[17] L. Yin, J. M. Moon, J. R. Sempionatto, M. Lin, M. Cao, A. Trifonov, F. Zhang, Z. Lou, J. -M. Jeong, S. -J. Lee, S. Xu, J. Wang, *Joule* **2021**, *5*, 1888.

[18] Y. Yu, J. Nassar, C. Xu, J. Min, Y. Yang, A. Dai, R. Doshi, A. Huang, Y. Song, R. Gehlhar, A. D. Ames, W. Gao, *Sci. Robot.* **2020**, *5*, eaaz7946.

[19] A. J. Bandodkar, P. Gutruf, J. Choi, K. Lee, Y. Sekine, J. T. Reeder, W. J. Jeang, A. J. Aranyosi, S. P. Lee, J. B. Model, R. Ghaffari, C. J. Su, J. P. Leshock, T. Ray, A. Verrillo, K. Thomas, V. Krishnamurthi, S. Han, J. Kim, S. Krishnan, T. Hang, J. A. Rogers, *Sci. Adv.* **2019**, *5*, eaav3294.

[20] R. Feiner, T. Dvir, *Nat. Rev. Mater.* **2018**, *3*, 17076.

[21] S. P. Lacour, G. Courtine, J. Guck, *Nat. Rev. Mater.* **2016**, *1*, 16063.

[22] S. P. Nichols, A. Koh, W. L. Storm, J. H. Shin, M. H. Schoenfisch, *Chem. Rev.* **2013**, *113*, 2528.

[23] Y. Liu, W. Huang, *Angew. Chem., Int. Ed.* **2021**, *60*, 2757.

[24] C. Jiang, G. Wang, R. Hein, N. Liu, X. Luo, J. J. Davis, *Chem. Rev.* **2020**, *120*, 3852.

[25] G. S. Wilson, M. A. Johnson, *Chem. Rev.* **2008**, *108*, 2462.

[26] Y. Huang, T. Masuda, M. Takai, *ACS Appl. Polym. Mater.* **2021**, *3*, 631.

[27] X. Xie, J. C. Doloff, V. Yesilyurt, A. Sadraei, J. J. McGarrigle, M. Omami, O. Veiseh, S. Farah, D. Isa, S. Ghani, I. Joshi, A. Vegas, J. Li, W. Wang, A. Bader, H. H. Tam, J. Tao, H. J. Chen, B. Yang, K. A. Williamson, J. Oberholzer, R. Langer, D. G. Anderson, *Nat. Biomed. Eng.* **2018**, *2*, 894.

[28] J. S. Del Rio, O. Y. F. Henry, P. Jolly, D. E. Ingber, *Nat. Nanotechnol.* **2019**, *14*, 1143.

[29] J. S. Yan, M. Orecchioni, F. Vitale, J. A. Coco, G. Duret, S. Antonucci, S. S. Pamulapati, L. W. Taylor, O. S. Dewey, M. D. Sante, A. M. Segura, C. Gurcan, F. D. Lisa, A. Yilmazer, M. D. McCauley, J. T. Robinson, M. Razavi, K. Ley, L. G. Delogu, M. Pasquali, *Carbon* **2021**, *173*, 462.

[30] L. Wang, S. Xie, Z. Wang, F. Liu, Y. Yang, C. Tang, X. Wu, P. Liu, Y. Li, H. Saiyin, S. Zheng, X. Sun, F. Xu, H. Yu, H. Peng, *Nat. Biomed. Eng.* **2020**, *4*, 159.

[31] Q. Gong, Y. Yu, L. Kang, M. Zhang, Y. Zhang, S. Wang, Y. Niu, Y. Zhang, J. Di, Q. Li, J. Zhang, *Adv. Funct. Mater.* **2021**, *32*, 2107360.

[32] F. Vitale, S. R. Summerson, B. Aazhang, C. Kemere, M. Pasquali, *ACS Nano* **2015**, *9*, 4465.

[33] L. Lu, X. Fu, Y. Liew, Y. Zhang, S. Zhao, Z. Xu, J. Zhao, D. Li, Q. Li, G. B. Stanley, X. Duan, *Nano Lett.* **2019**, *19*, 1577.

[34] X. Wu, J. Feng, J. Deng, Z. Cui, L. Wang, S. Xie, C. Chen, C. Tang, Z. Han, H. Yu, X. Sun, H. Peng, *Sci. China Chem.* **2020**, *63*, 1281.

[35] C. B. Jacobs, I. N. Ivanov, M. D. Nguyen, A. G. Zestos, B. J. Venton, *Anal. Chem.* **2014**, *86*, 5721.

[36] W. Jia, G. Valdés-Ramírez, A. J. Bandodkar, J. R. Windmiller, J. Wang, *Angew. Chem., Int. Ed.* **2013**, *52*, 7233.

[37] J. Wang, *Chem. Rev.* **2008**, *108*, 814.

[38] H. Teymourian, A. Barfidokht, J. Wang, *Chem. Soc. Rev.* **2020**, *49*, 7671.

[39] P. N. Bartlett, F. A. Al-Lolage, *J. Electroanal. Chem.* **2018**, *819*, 26.

[40] H. Lee, S. M. Dellatore, W. M. Miller, P. B. Messersmith, *Science* **2007**, *318*, 426.

[41] A. B. Asha, Y. Chen, R. Narain, *Chem. Soc. Rev.* **2021**, *50*, 11668.

[42] L. Lu, Y. Zhou, J. Pan, T. Chen, Y. Hu, G. Zheng, K. Dai, C. Liu, C. Shen, X. Sun, H. Peng, *ACS Appl. Mater. Interfaces* **2019**, *11*, 4345.

[43] I. Terem, L. Dang, A. Champagne, J. Abderezaei, A. Pionteck, Z. Almadan, A.-M. Lydon, M. Kurt, M. Scadeng, S. J. Holdsworth, *Magn. Reson. Med.* **2021**, *86*, 1674.

[44] A. Zebda, J. P. Alcaraz, P. Vadgama, S. Shleev, S. D. Minteer, F. Boucher, P. Cinquin, D. K. Martin, *Bioelectrochemistry* **2018**, *124*, 57.